Vol. 24, No. 2(2025) Mat25518
Revista Mexicana de Ingeniería Química

3D printing of microchannels with MSLA technology for microfluidic devices: From design to manufacturing

Impresión 3D de microcanales con tecnología MSLA para dispositivos microfluídicos: del diseño a la fabricación

E.G. Rivera-Medellin[1,2], I. Pereyra-Laguna[3], L.E. Lugo-Uribe[4], M.A. González-López[3*], J. Mayen-Chaires[3*]
[1]*Posgrado CIATEQ, A.C., Eje 126 No. 225, Zona Industrial San Luis C.P. 78395 San Luis Potosí, SLP, México.*
[2]*Universidad Tecnológica de San Luis Potosí, Prol. Av. Dr. Arturo Nava Jaimes, Rancho Nuevo, Soledad de Graciano Sánchez, SLP.*
[3]*CIATEQ, A.C., Centro de Tecnología Avanzada, Eje 126 No. 225, Zona Industrial, 78395, San Luis Potosí, SLP, México.*
[4]*CIATEQ, A.C., Centro de Tecnología Avanzada. 52004, Estado de México, Lerma, México.*
Received: January 30, 2025; Accepted: March 27, 2025

Abstract
Microfluidics has gained prominence in recent decades due to its ability to manipulate fluids through micrometric channels and perform analyses comparable to those of a full laboratory. Applications span fields such as chemistry and neuroscience. However, one of the main challenges is the fabrication process, which is often expensive and requires specialized facilities. This study aims to design and fabricate microfluidic devices with microchannels that achieve high concordance between the design and the final product, using a low-cost MSLA 3D printer. Variables such as microchannel width and height, along with printing parameters like exposed layer height and exposure time, were evaluated. The fabricated samples were analyzed using a KEYENCE microscope equipped with a VH-20R RZ x20–x200 lens. A design of experiments was conducted to optimize the variable levels, resulting in ideal printing parameters. The findings demonstrate that this technology enables the fabrication of functional microchannels for microfluidic devices, offering an affordable and efficient alternative to traditional methods. This approach has the potential to broaden access to microfluidic technology.
Keywords: microfluidics, microchannels, MSLA 3D printing, area compliance, design of experiments.

Resumen
La microfluídica ha cobrado relevancia en las últimas décadas por su capacidad de manipular fluidos a través de canales micrométricos y realizar análisis similares a los de un laboratorio. Sus aplicaciones abarcan campos tan diversos como la química y la neurociencia. Sin embargo, uno de los mayores retos es su fabricación, que suele ser costosa y requerir instalaciones especializadas. Este estudio tiene como objetivo diseñar y fabricar dispositivos microfluídicos con microcanales que logren alta concordancia entre el diseño y el producto final, empleando una impresora 3D de tecnología MSLA de bajo costo. Se evaluaron variables como el ancho y la altura de los microcanales, junto con parámetros de impresión como la altura de capa expuesta y el tiempo de exposición. Las muestras fabricadas fueron analizadas con un microscopio KEYENCE equipado con un lente VH-20R RZ x20–x200. Mediante un diseño de experimentos, se optimizaron los niveles de las variables, obteniendo parámetros de impresión ideales. Los resultados muestran que esta tecnología permite fabricar microcanales funcionales para dispositivos microfluídicos, ofreciendo una alternativa económica y eficiente frente a los métodos tradicionales, con el potencial de ampliar el acceso a esta tecnología.
Palabras clave: microfluídica, microcanales, impresión 3D MSLA, cumplimiento del área, diseño de experimentos.

*Corresponding author. *E-mail*: dcmiguelgl@gmail.com; dr.jmayen@gmail.com ;
https://doi.org/10.24275/rmiq/Mat25518
ISSN:1665-2738, *issn-e*: 2395-8472

1 Introduction

Microfluidics is a technology designed to manipulate fluids in channels with dimensions in the range of tens of micrometers (Whitesides, 2006). Due to its applicability in diverse research areas such as chemistry, medicine, and physics, this technology has evolved rapidly (Bragheri *et al*., 2019). It enables the processing of extremely small fluid volumes (10^{-9} to 10^{-18} L) using channels at the micrometer scale (Niculescu *et al*., 2021; Ren *et al*., 2013). This technology is succinctly described by the term "lab-on-a-chip" (Dietzel Andreas, 2016), which illustrates how a small device, considered a chip, can encompass the analytical functions, capabilities, and applications of a complete laboratory (Dittrich & Manz, 2006). Additional research highlights the growing importance of microfluidics in bioseparations, emphasizing its ability to enhance analytical processes by reducing reagent consumption and processing times (Lapizco-Encinas, 2008). Microfluidics is also employed for culturing neuronal populations, acting as a guide for neurites and providing tools to dissect the spatiotemporal complexity of normal development and the establishment of brain circuits in vitro. This has popularized the use of such tools as neuronal microenvironments (Kajtez *et al*., 2020; Taylor *et al*., 2003).

However, this technology faces significant challenges, particularly in the manufacturing of microfluidic devices. Some of these devices are fabricated through photolithography, a process that involves harmful chemicals and requires expensive facilities meeting Class 10/ISO4 cleanliness standards (US FED STD 209E Cleanroom Standards) (Mukherjee *et al*., 2019). Additionally, the high production costs associated with substrate materials and material removal techniques contribute to significant waste generation. Scalability also remains a critical issue. Recent studies have explored alternative fabrication approaches, including dielectrophoresis-based techniques, which offer potential advantages in manipulating biological samples and improving separation efficiency at the microscale (Garza-García & Lapizco-Encinas, 2010).

The fabrication processes for these devices can be classified into material removal techniques and material addition techniques, as shown in Figure 1. Material removal techniques, such as electrical discharge machining (EDM), direct laser machining, engraving techniques, CNC machining, and soft lithography, create structures by eliminating material from a bulk substrate. While these approaches offer precision and versatility, they inherently generate material waste, require specialized equipment, and involve multi-step processes that increase costs.

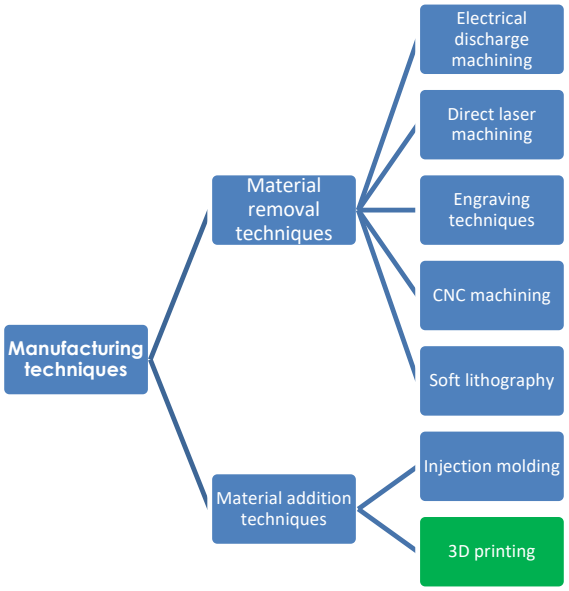

Figure 1.Microfluidic device fabrication process.

Conversely, material deposition techniques, such as stereolithography (SLA), inkjet 3D printing, and direct writing, construct structures by adding material layer by layer. These methods are generally more material-efficient, allow for rapid prototyping, and enable complex geometries, but may also present surface roughness challenges and limitations in fabricating fully enclosed channels (Waldbaur *et al*., 2011).

Among material deposition methods, MSLA 3D printing has emerged as a promising alternative for microfluidic device fabrication. Unlike soft lithography, which requires cleanroom environments, elastomeric molding, and multi-step fabrication (Talam *et al*., 2025), or CNC machining, which often struggles with high-resolution enclosed microchannels, MSLA enables the direct fabrication of custom-designed microchannels with high reproducibility and significantly reduced material waste (Garza-García & Lapizco-Encinas, 2010). While soft lithography remains ideal for applications requiring highly flexible substrates, and CNC machining excels in rigid open-channel designs, MSLA provides a balance between cost efficiency, precision, and accessibility. Recent studies have demonstrated that, with proper optimization, MSLA 3D printing can achieve dimensional compliance close to 100%, making it a viable alternative for rapid prototyping and scalable microfluidic applications (Liu *et al*., 2024).

In recent years, additive manufacturing has made significant advancements, enabling high-resolution fabrication of microparts. Some of these technologies include selective laser sintering (SLS) (Wei & Li, 2021) and two-photon polymerization (TPP) (Zhou *et al*., 2015). These systems offer exceptional resolution, but their high cost and limited scalability restrict their broader implementation (Gibson *et al*., 2010).

MSLA 3D printing, on the other hand, provides a low-cost, scalable solution that bridges the gap between traditional and modern fabrication techniques, making it an ideal choice for microfluidic research and prototyping.

Conversely, material addition techniques, such as injection molding, rely on the deposition or formation of material to construct the required components. Among these approaches, 3D printing emerges as a pivotal technology due to its versatility, customization capabilities, and potential to reduce both costs and material waste.

In recent years, additive manufacturing has made significant advancements, enabling high-resolution fabrication of microparts. Some of these technologies include selective laser sintering (SLS) and two-photon polymerization (TPP) (Zhou *et al*., 2015). These systems are ideal for device fabrication due to their high resolutions; however, their high cost limits their scalability for mass production. In addition, the integration of microscale cell analysis techniques in microfluidic platforms has been widely studied, providing insights into their application in fields such as biotechnology and biomedical research (Sósol-Fernández *et al*., 2012).

Recently, desktop 3D printers have emerged, now widely used for product customization (Shahrubudin *et al*., 2019). These printers offer great flexibility and good resolution at low cost (Leong *et al*., 2024). Examples of 3D printing technologies include SLA (stereolithography) (Manapat *et al*., 2017) , DLP (digital light processing) (Zhang *et al*., 2020), MSLA (masked stereolithography) (Borra & Neigapula, 2023), and CLIP (continuous liquid interface projection) (Tumbleston *et al*., 2015). The principle behind these technologies involves slicing the 3D model into 2D layers, which are then solidified layer by layer, typically along the z-axis, through a resin photopolymerization process until the entire piece is formed.

To fully leverage the advantages of 3D printing in microfluidic device fabrication, the design process plays a crucial role, requiring the integration of advanced software tools and precise modeling techniques. Computer-aided design (CAD) software has been widely used for 3D modeling in various fields such as engineering, mechanics, technology, electronics, and architecture. More recently, it has been applied to the development of 3D-printed components (Junk & Kuen, 2016). These tools allow precise design of models with ideal dimensional parameters, enabling the creation of microchannels with scales smaller than 100 μm (Autodesk.com, n.d.).

Once the design is complete, it must be exported to the STL format (STereoLithography), which is considered the standard for data exchange in additive manufacturing. This conversion involves running a surface triangulation algorithm commonly used in finite element methods. Process planning includes steps such as dividing the part's surfaces into triangles, generating trajectories for each layer. This data conversion produces a standardized language known as G-code, used in additive manufacturing and CNC machining to control machine movements and operations (Topcu & Unver, 2011).

This research aims to establish manufacturing principles for fabricating microfluidic devices capable of fluid transport and analysis using MSLA 3D printing technology. This approach leverages its high commercial availability and flexibility for low-cost prototyping. Variables such as layer height, exposure time, channel width, and channel depth are analyzed using a full factorial experimental design.

2 Material and methods

For this study, a commercial standard (brand: e-sun, transparent standard) with a liquid density of 1.08–1.13 g/cm^3 was used. The 3D resin printer utilized was an Elegoo Saturn 3 12K, with a resolution of 19 × 24 μm, equipped with a 10-inch monochrome 12K LCD screen operating at a wavelength of 405 nm and a build volume of 218.88 mm (length) × 122.88 mm (width) × 250 mm (height). The cleaning of the printed parts was performed using a Solv 3D washer with isopropyl alcohol. The characterization of the printed samples was conducted using a KEYENCE VHX-970F digital optical microscope, equipped with a VH-20R lens (magnification range: x20 - x200). The general method used is depicted in Figure 2.

Initially, the geometry of the channels was defined, and the design was created using Autodesk Fusion. The printing parameters were then configured in the slicing software. Test specimens were subsequently printed and washed with isopropyl alcohol. Excess alcohol was removed using compressed air. Each specimen was labelled and individually packed. Finally, the printed parts were characterized using the microscope, and the data were analyzed statistically.

2.1 Microchannel design

The experimental test specimen designed for this study measured 50 mm in length, 21 mm in width, and 5 mm in height. It contained 12 open microchannels. This design choice was informed by previous studies reporting that closed channels fabricated at dimensions <300 μm often become clogged with resin(Ahmed *et al*., 2022)**.** The microchannels were grouped into four clusters with varying dimensions and characteristics, as described below.

Figure 2. Method for printing microchannel samples.

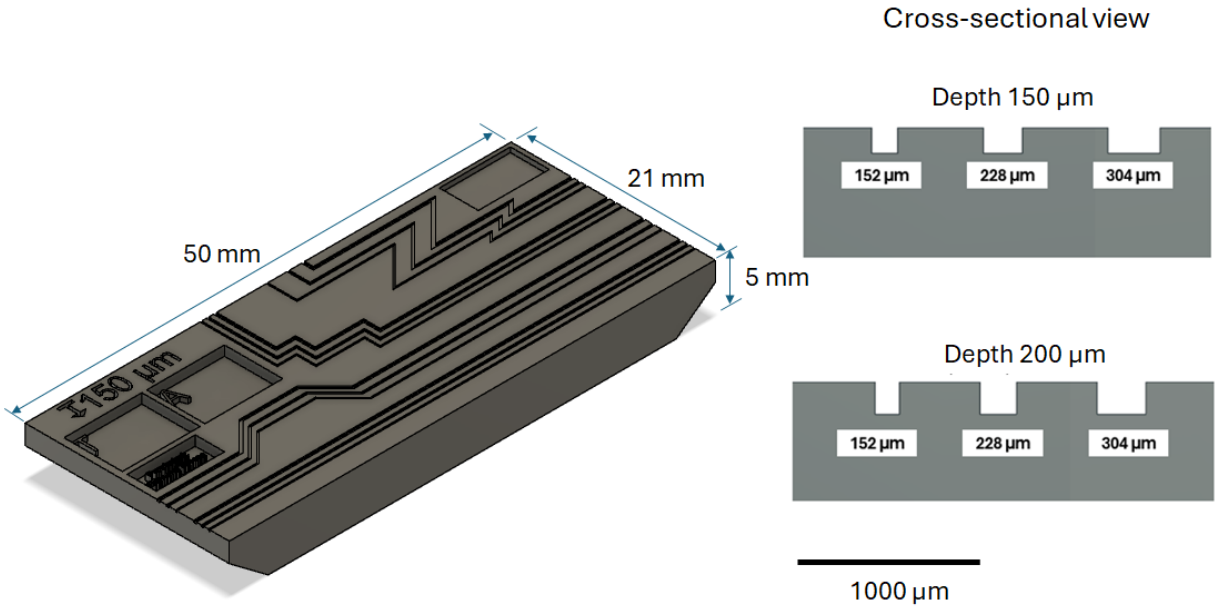

Figure 3. Dimensions of channel cross-sectional area.

The cross-sectional geometry of the channels as seen in Figure 3 was defined as a rectangular shape pattern, given the nature of the MSLA 3D printing process. In this method, the pixels of the LCD screen define the shape of the layer being photopolymerized, making additive manufacturing a viable microfabrication process (J. F. Blinn, 2005; Gao *et al*., 2023; Mishra, 2020; Tabeling, 2023)

The channel dimensions were determined based on the advancement of the build plate along the z-axis for depth and along the x- and y-axes for width. These dimensions were referenced from pixel multiples as established by Leong *et al*. (2024) in their experiments. For the printer used in this study, the pixel dimensions were 19 μm in the x-axis, 24 μm in the y-axis, and a minimum step of 10 μm in the z-axis. Consequently, channels with two different depths (150 μm and 200 μm) and three different widths (152 μm,

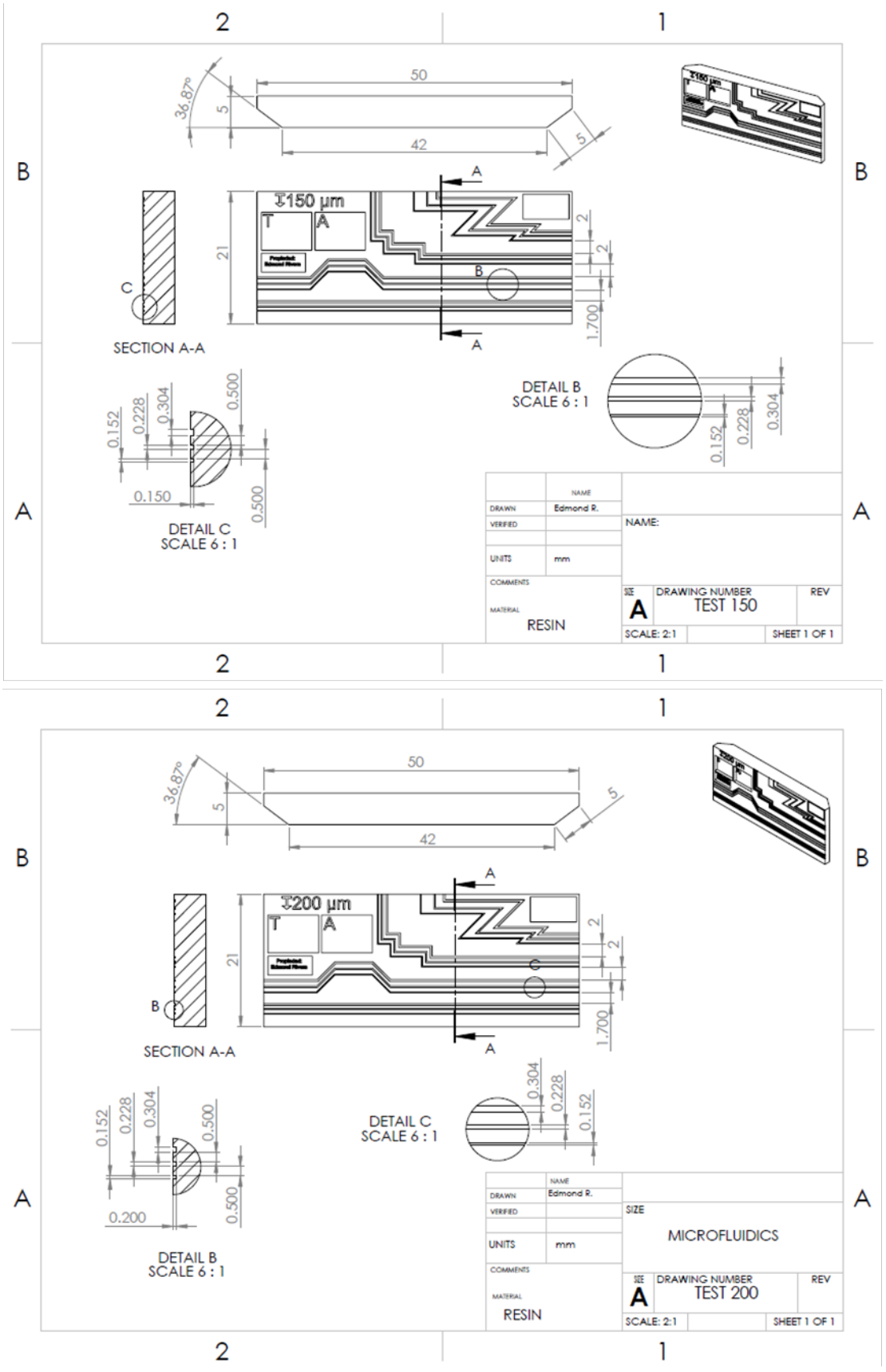

Figure 4. Microchannel sample diagrams according to ISO standard.

228 μm, and 304 μm) were evaluated, corresponding to pixel counts of 8, 12, and 16 along the x-axis, respectively, as shown in Figure 3. These dimensions align with the ranges reported in prior studies by Leong *et al*. (2024)(34.4 to 309.6 nm) and Razavi Bazaz *et al*. (2020) (40 to 300 μm).

The details of the test samples are presented in the schematics under the ISO standard shown in Figure 4.

2.2 Printing parameters

The printing parameters were based on the specifications provided by the slicing software, as shown in Table 1. However, two parameters identified in the study by Leong *et al*. (2024), were found to influence the resolution of the microchannel significantly. These variables were layer height, where the minimum height allowed by the printer is 10 μm. Based on this, three levels were selected: 20 μm, 30 μm, and 50 μm, taking 50 μm as a reference from the study by Orzeł& Stecuła (2022). The second variable was the UV exposure time for each layer to solidify, with the levels set at 1.5 s, 1.8 s, and 2 s (Leong *et al*., 2024; Valizadeh *et al*., 2023).

Table 1. Parameters for printing.

Parameter	Value	Unit
Layer height	0.02 & 0.03 & 0.05	mm
Total lower layers	10	
Exposure Time	1.5 & 1.8 & 2	s
Bottom Exposure Time	20	s
Transition Layer Count	8	
Machine type	Linear	
Transition Decrement	2	s
Printing standby mode	Time	
Ascend descent time	0	s
Retreat descent time	0.5	s
Bottom Lift Distance	3 + 4	mm
Lifting Distance	3	mm
Bottom lift distance	5.5	mm
Retraction distance	5.5	mm
Lower lifting speed	65 & 180	mm/min
Lifting Speed	65	mm/min
Retraction speed	180 & 65	mm/min

2.3 Printing process

The first step involved calibrating the build plate as specified by the manufacturer. The resin was poured to the specified level, and the printer's cover was closed. The preloaded program was selected from the printer's memory, and printing commenced. The process was conducted within a temperature range of 23 and 26°C (+/- 0.3°C), (Ahmed *et al*., 2022; Kaufmann *et al*., 2024; Milovanović *et al*., 2024).

2.4 Post-processing: Washing procedure

Each specimen took between 40 and 90 minutes to print. After detaching the printed part from the building plate, it was placed in a washing station containing isopropyl alcohol. The washing process lasted 5 minutes and involved the rotation of internal blades, which stirred the isopropyl alcohol to ensure thorough cleaning of the printed structures.

Following the washing process, compressed air was applied for 30 seconds to remove any residual isopropyl alcohol from the surface of the printed parts (Collingwood *et al*., 2023), ensuring proper post-processing before characterization. Each specimen was labelled and accompanied by a registration sheet for individual storage.

2.5 Experimental design

The experimental design employed was a full factorial design with multiple levels to evaluate the influence of various variables and their interactions. Table 2 summarizes the Design of Experiments (DOE) approach (Niedz & Evens, 2016), based on the described variables.

The first factor was the UV exposure time, which had three levels: 1.5, 1.75, and 2 s. The second factor was the layer height, also with three levels: 20 μm, 30 μm, and 50 μm. The third factor was the channel width, with three levels: 152 μm, 228 μm, and 304 μm. The final factor was the channel depth, with two levels: 150 μm and 200 μm. Five samples were taken for each combination of factors.

Table 2. Summary of DOE.

Element	Value
Factors	4
Replicas	5
Base runs	54
Total runs	270
Base blocks	1
Total blocks	1
Number of levels	3, 3, 3, 2

The direct output variables measured using the microscope included the cross-sectional area, maximum channel depth, and roughness. These output variables were used to calculate the average channel width, the percentage compliance of the designed cross-sectional area compared to the fabricated area, and the percentage compliance of the designed depth compared to the fabricated depth. This indicator was calculated using Equation 1, as described in the literature (Torres-Alvarez *et al*., 2024).

$$\%\ Cross-sectional\ area\ compliance = \left(\frac{Fabricated\ cross-sectional\ area}{Designed\ cross-sectional\ area}\right)\times 100 \quad (1)$$

This indicator is essential as it provides a value reflecting the degree of compliance between the

fabricated and designed cross-sectional areas. Since this is expressed as a percentage, the response and optimization of the variables and their levels are consistent across all designed cross-sectional sizes.

Similarly, the percentage compliance of the designed depth compared to the fabricated depth was also considered, using Equation 2.

$$\%\ Depth\ Compliance = \left(\frac{Fabricated\ depth}{Designed\ depth}\right) \quad (2)$$

3 Results

The specimens appeared to have permeable channels. In Figure 5a, a complete image of the specimen is shown, highlighting well-defined channels. Figure 5b presents a magnified view of the channels, while Figure 5c provides a 3D reconstruction of a segment selected for measurement.

The specimens were measured using a microscope in the areas indicated in Figure 6a. Random sampling was performed in the specified zones, and the images obtained were from the straight sections of the channels. The microscope allowed for the acquisition of three-dimensional images of the segments to be measured, as shown in Figures 5c and 6a. This 3D reconstruction made it possible to section the image and obtain measurements of the cross-sectional dimensions. Five measurements were taken for each segment of every channel.

The cross-sectional height and area were measured in these sections, with the cross-sectional area highlighted in pink in Figure 6b.

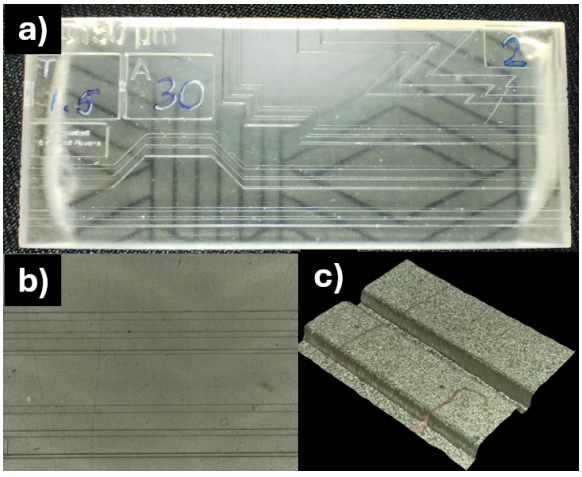

Figure 5. a) Test device image, b) expansion of a segment, and c) reconstruction of a segment of a microchannel.

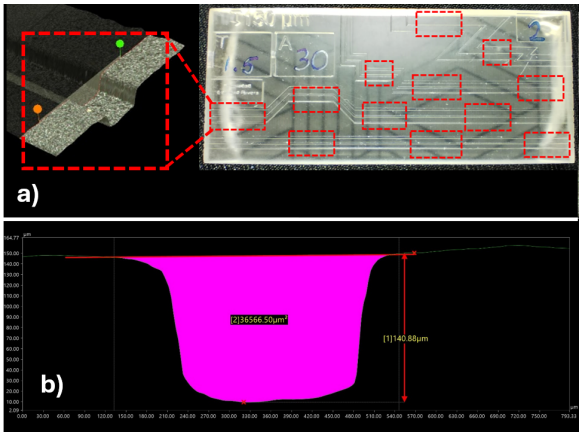

Figure 6. a) Indicated areas where characterization is carried out in a test device microchannels and 3D reconstruction of the microchannel, and b) cross-sectional area of the channel.

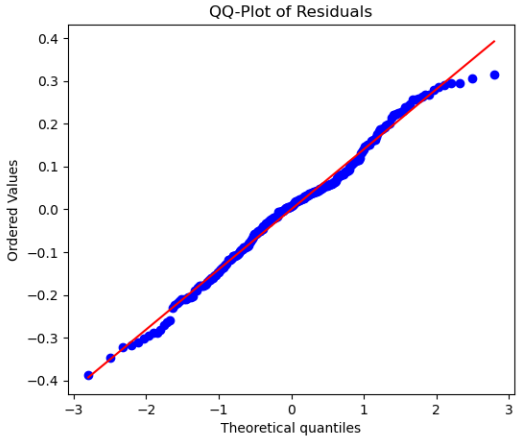

Figure 7. Normal probability plot.

3.1 *Factorial design analysis*

The data obtained from the microscope were statistically analyzed using a full factorial design. Figure 7 presents the normal probability plot for the cross-sectional area compliance percentage, showing a linear correlation and normal behavior.

An analysis of variance (ANOVA) was conducted for the main factors, with results presented in Table 3. It was observed that the most significant contributors to the variation in the microchannel's cross-sectional area were layer height and channel width (X-axis), as indicated by their F-values.

The model summary indicates a standard error (S) of 0.129233. The R-squared value is 72.93%. The adjusted R-squared is slightly lower, at 72.20%, accounting for the number of predictors in the model. Finally, the predicted R-squared value is 71.25%.

Given that the p-value obtained is less than 0.001, with a confidence level of 90%, it can be assumed that there is a relationship between the variables: exposure time, layer height, channel width, and depth,

Table 3. Analysis of variance.

Source	DF	Adj SS	Adj MS	F-Value	P-Value
Model	7	11.7876	1.68394	100.83	0
Linear	7	11.7876	1.68394	100.83	0
Exposure Time	2	1.0577	0.52885	31.67	0
Layer height	2	6.6199	3.30996	198.19	0
Chaneel width (X)	2	4.0466	2.02329	121.15	0
Depth (Z)	1	0.0634	0.06336	3.79	0.053
Error	262	4.3757	0.0167		
Lack-of-Fit	46	4.1555	0.09034	88.62	0
Pure Error	216	0.2202	0.00102		
Total	269	16.1633			

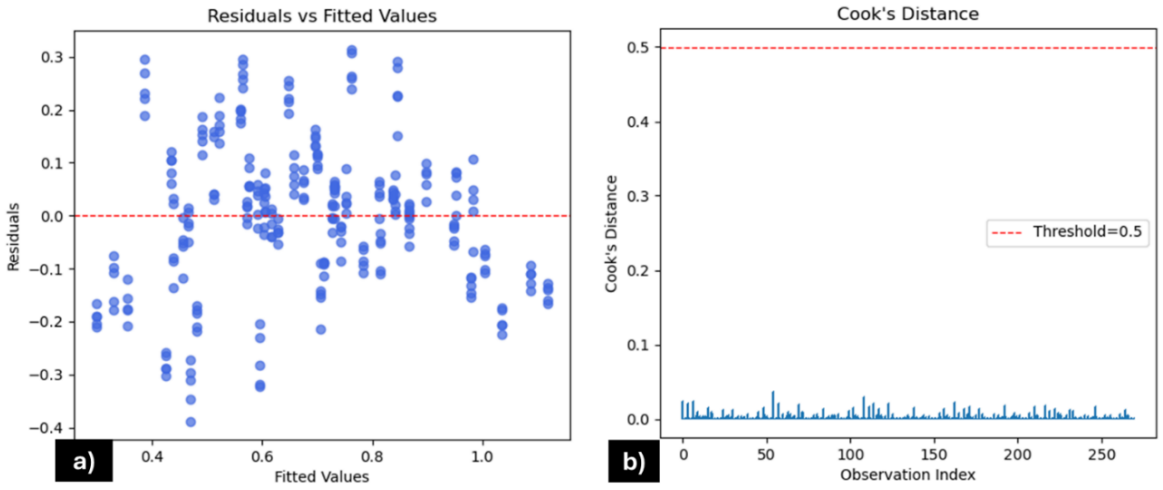

Figure 8. a) Residuals vs Fitted Values for area compliance percentage. b) Cook's distance plot.

according to the statistical study. Derived from the multiple regression analysis for cross-sectional area compliance, an R-squared value of 78.49% was achieved, indicating that a significant proportion of the variation in compliance is explained by the input variables (layer height, exposure time, channel width, and depth). A higher percentage indicates a better fit of the regression model to the observed data.

The 270 samples obtained from the experiment are sufficient to achieve an accurate estimation of the relationship between the variables. As shown in the scatter plot in Figure 8a, the values appear to be randomly distributed. Furthermore, using Cook's Distance (Figure 8b), no point exceeds the threshold (indicated by the red dashed line), meaning there are no outliers that could negatively impact the model.

According to the Shapiro-Wilk test, where:

- H_0: The distribution is normal
- H_1: The distribution is not normal,

With a significance level of 0.5, the resulting p-value is 0.0662. Therefore, the normality of the data is accepted.

3.2 *Main effects and trends*

In the main effects plot (Figure 10) for the adjusted mean compliance percentage of the cross-sectional area, the factor with the greatest influence on this variable is layer height. A positive trend is observed, indicating that increasing layer height results in higher compliance percentages. Similarly, channel width exhibits a positive correlation, suggesting that wider channels yield higher compliance percentages for the cross-sectional area.

Conversely, exposure time per layer shows a negative correlation, meaning that shorter exposure times result in higher compliance percentages. Finally, channel depth exhibits a slight negative trend.

3.3 *Interactions and optimization analysis*

Figure 10a presents an interaction plot for the factors affecting the percentage compliance of the cross-sectional area in adjusted means. For the interaction between exposure time and layer height, the condition yielding the highest compliance percentage is a combination of an exposure time of 1.5 seconds and a layer height of 50 μm.

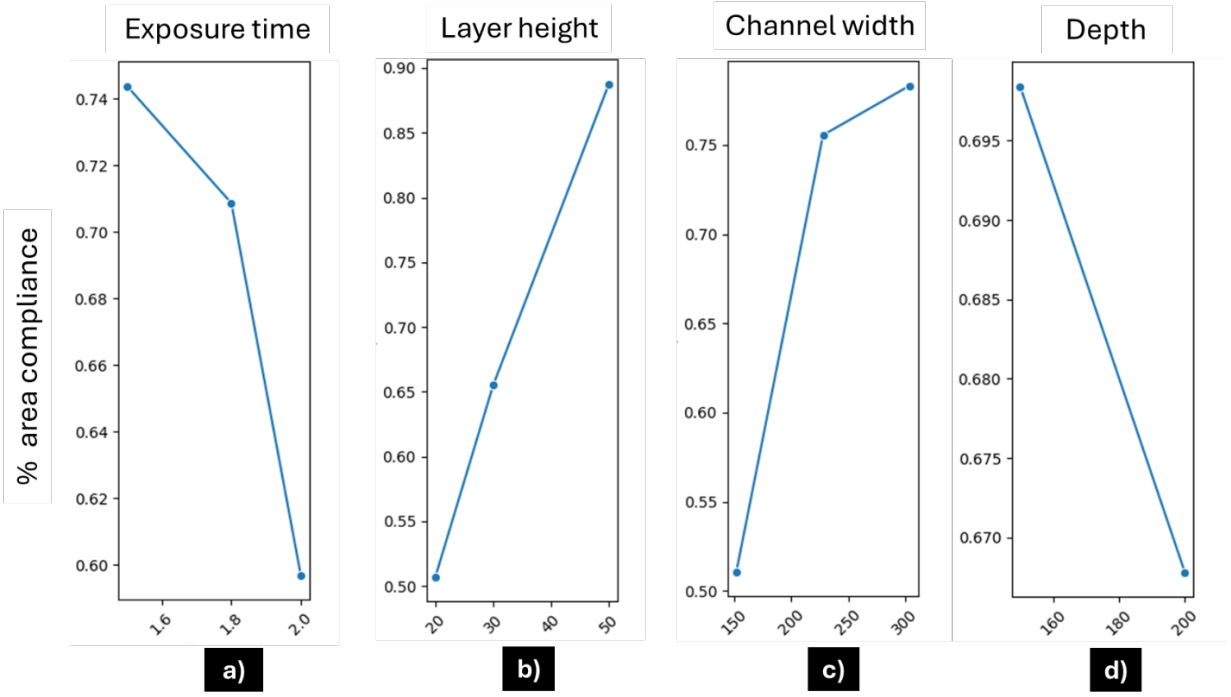

Figure 9. Main effects graph of area compliance with input variables.

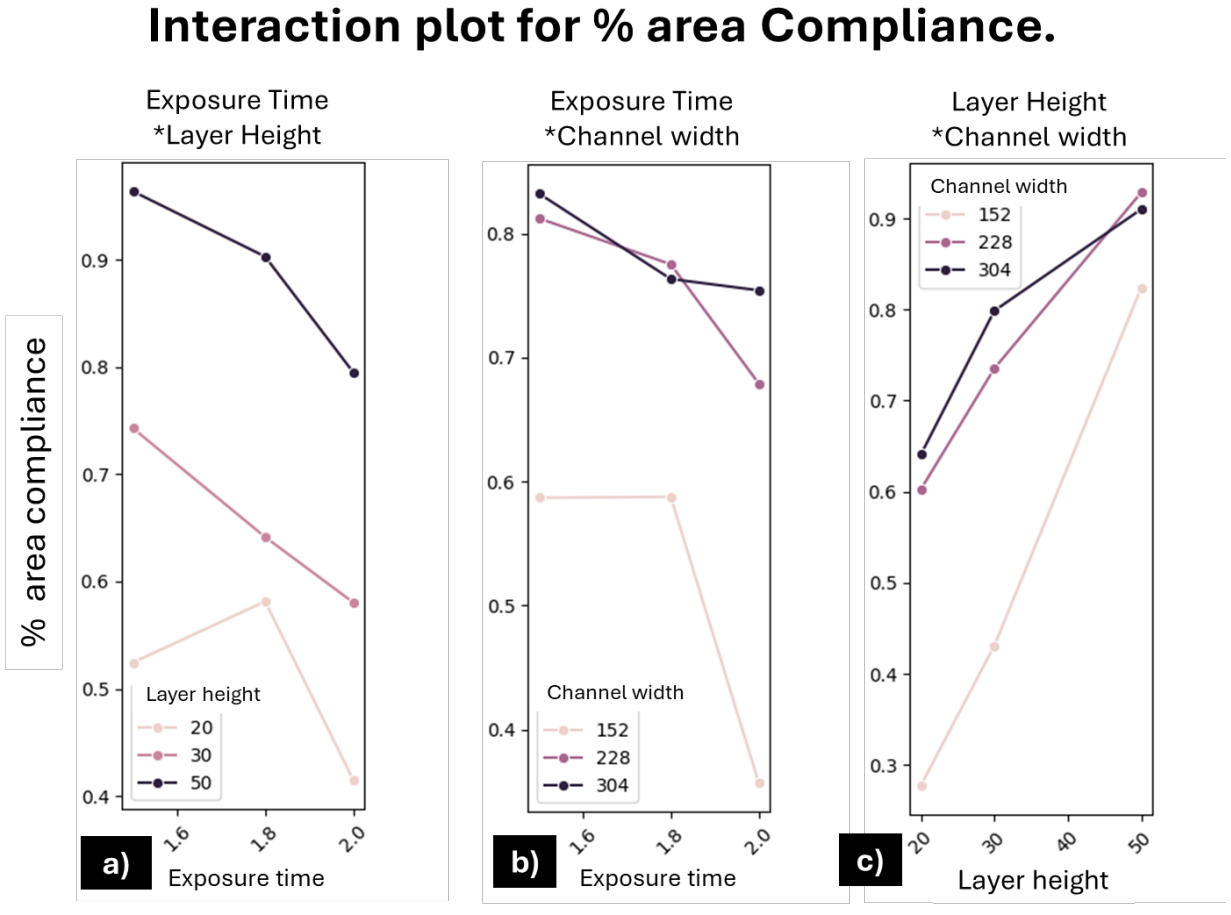

Figure 10. Interactions of input variables against printed area compliance.

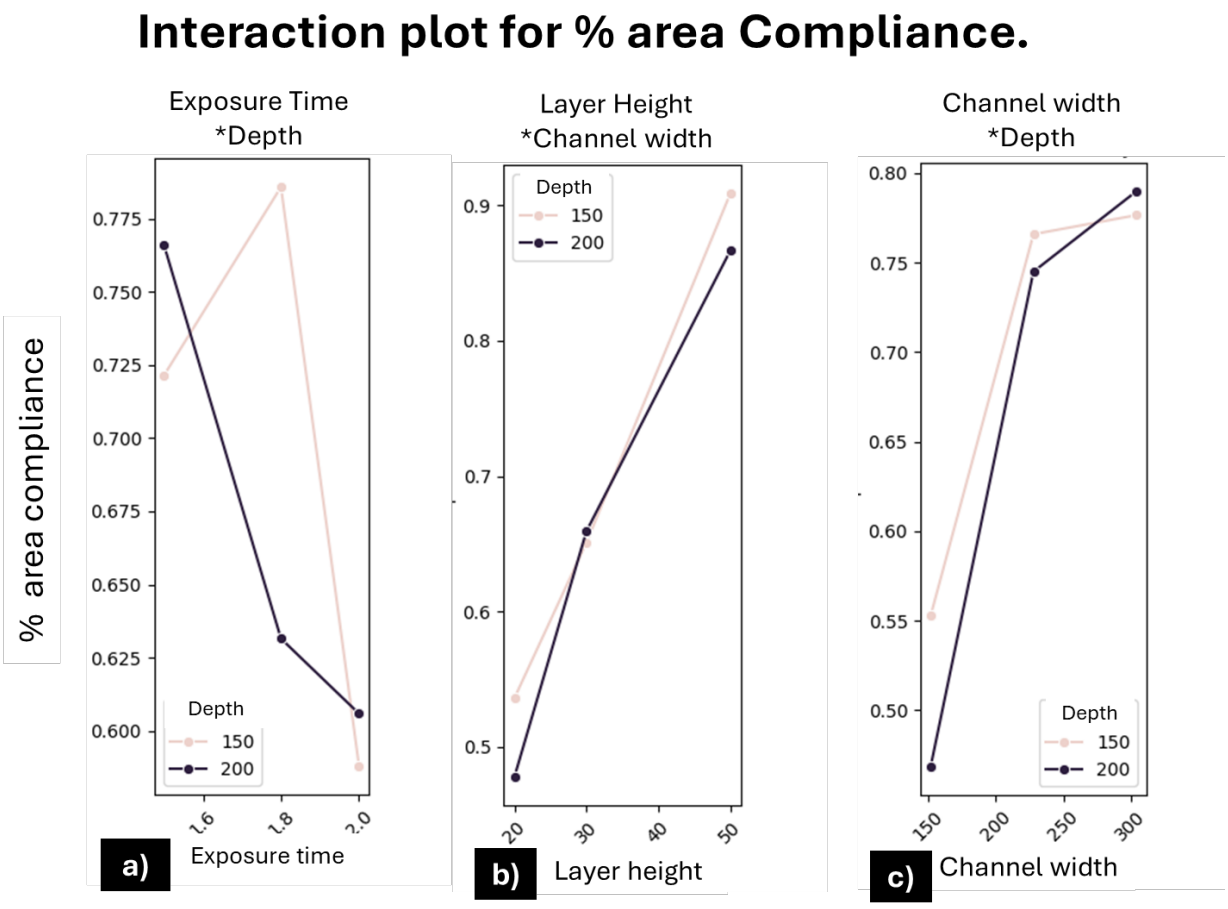

Figure 11. Interactions of input variables against printed area compliance.

In the interaction between exposure time and channel width Figure 10b, the behavior is similar for channel widths of 228 μm and 304 μm. However, the exposure time of 1.5 seconds still provides the highest area compliance in this interaction.

For the interaction between layer height and channel width Figure 10c, a similar trend is observed for channels with widths of 228 μm and 304 μm. However, higher layer heights lead to better compliance percentages for the cross-sectional area.

In the interaction between exposure time and depth 11a, the behavior is consistent at 1.5 and 2 seconds, with a slight variation observed for the 1.8-second exposure time at a depth of 150 μm.

For the interaction between layer height and depth Figure 11b and 11c, both depths exhibit similar trends, as does the interaction between channel width and depth, which shows a positive trend.

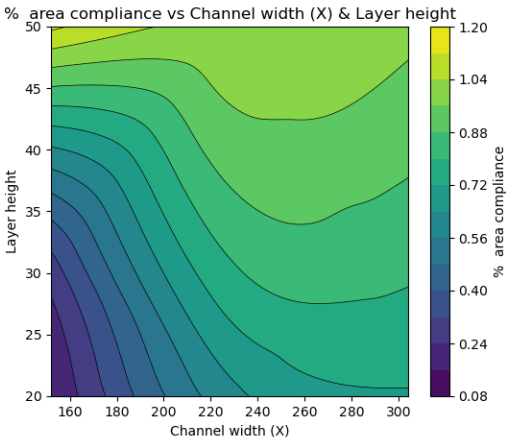

Figure 12. Area contour plot for percentage compliance of cross-sectional area vs layer height and channel width.

3.4 Contour plot and prediction

The contour plot in Figure 12 shows that when variables are set to a layer height of 50 μm and a channel width exceeding 300 μm, the probability of achieving nearly 100% compliance in the cross-sectional area increases significantly.

Using optimization and prediction statistics, the predictor "Y" achieved a maximized compliance value of 1.11805, exceeding 100%, indicating an area larger than the specified design. This optimal solution, suggested by the software, is achieved with the following parameters:

- **X1 (Exposure time):** 1.5 s
- **X2 (Layer height):** 50 μm
- **X3 (Channel width):** 304 μm
- **X4 (Depth):** 150 μm

Other possible solutions according to statistical optimization, closer to 100% compliance are shown below

Solution 1: X1 = 1.8 s, X2 = 50 μm, X3 = 304 μm, X4 = 200 μm

Solution 2: X1 = 1.5 s, X2 = 50 μm, X3 = 228 μm, X4 = 150 μm

These two solutions encompass a range where 100% optimization of the microchannel's cross-sectional area is achieved. Based on these predictions, future experiments with a larger sample size are planned to validate these results.

Conclusions

This study demonstrates the feasibility of fabricating microchannels for microfluidic devices using MSLA 3D printing technology. The experimental results validate the effectiveness of this approach in achieving high-resolution microfabrication, highlighting its potential for broader applications beyond specific printer models.

As discussed throughout this work, the input factors—layer height, exposure time, and the channel dimensions (width and depth)—have a significant impact on the compliance of the cross-sectional area of the channels. Among these, layer height and channel width were identified as the most influential parameters, with a positive correlation to cross-sectional area compliance.

Moreover, it was observed that optimizing these factors can yield microchannels with cross-sectional areas achieving compliance levels very close to 100% of the designed specifications. The ability to reach such high accuracy underscores the potential of MSLA 3D printing technology in the precise manufacturing of microfluidic devices at a considerable low cost.

The findings also highlight the importance of using systematic experimental approaches, such as factorial designs, to identify optimal manufacturing conditions. This approach not only enables precise tuning of input parameters but also facilitates the identification of interactions between variables, which is critical in achieving optimal outcomes.

The successful fabrication of microchannels using a commercially available, cost-effective desktop 3D printer opens new possibilities for the democratization of microfluidic technology. However, future work should explore additional factors such as resin composition, post-processing techniques, and the mechanical properties of the printed devices. Furthermore, scaling up the sample size and conducting long-term reliability tests will be essential for establishing the robustness of the proposed manufacturing process.

Finally, this work demonstrates that additive manufacturing, particularly MSLA 3D printing, holds great promise in advancing the field of microfluidics at a very low cost, promoting a paradigm shift for sensing solutions in different specialized sectors such as medicine and environmental applications by democratization of these technologies. By enabling the fabrication of complex geometries with precision and repeatability, this technology can significantly contribute to the development of innovative solutions for fluid manipulation at the microscale.

References

Ahmed, I., Sullivan, K., & Priye, A. (2022). Multi-resin masked stereolithography (MSLA) 3D printing for rapid and inexpensive prototyping of microfluidic chips with integrated functional components. *Biosensors (Basel)*, *12*(8), 652. https://doi.org/10.3390/bios12080652

Autodesk.com. (n.d.). Presición de autodesk. In *Autodesk.com*. Retrieved December 28, 2024, from https://www.autodesk.com/mx/solutions/cad-software#:~:text=%C2%BFQu%C3%A9%20es%20el%20software%20de,y%20simular%20el%20rendimiento%20real

Blinn, J. F. (2005). What Is a Pixel? *IEEE Computer Graphics and Applications*, *25*(5), 82–87. https://doi.org/10.1109/MCG.2005.119

Borra, N. D., & Neigapula, V. S. N. (2023). Parametric optimization for dimensional correctness of 3D printed part using masked stereolithography: Taguchi method. *Rapid Prototyping Journal*, *29*(1), 166–184. https://doi.org/10.1108/RPJ-03-2022-0080

Bragheri, F., Vázquez, R. M., & Osellame, R. (2019). Microfluidics. In *Three-Dimensional Microfabrication Using Two-Photon Polymerization* (pp. 493–526). Elsevier. https://doi.org/10.1016/B978-0-12-817827-0.00057-6

Collingwood, J., De Silva, K., & Arif, K. (2023). High-speed 3D printing for microfluidics: Opportunities and challenges. *Materials Today:*

Proceedings. https://doi.org/10.1016/j.matpr.2023.05.683

Dietzel Andreas. (2016). *Microsystems for Pharmatechnology Manipulation of Fluids, Particles, Droplets, and Cells*.

Dittrich, P. S., & Manz, A. (2006). Lab-on-a-chip: Microfluidics in drug discovery. In *Nature Reviews Drug Discovery* (Vol. 5, Issue 3, pp. 210–218). https://doi.org/10.1038/nrd1985

Gao, H., An, J., Chua, C. K., Bourell, D., Kuo, C. N., & Tan, D. T. H. (2023). 3D printed optics and photonics: Processes, materials and applications. In *Materials Today* (Vol. 69, pp. 107–132). Elsevier B.V. https://doi.org/10.1016/j.mattod.2023.06.019

Garza-García, L. D., & Lapizco-Encinas, B. H. (2010). STATE OF THE ART ON PROTEIN MANIPULATION EMPLOYING DIELECTROPHORESIS. *Revista Mexicana de Ingeniería Química*, *2*(2), 1156–1741. https://rmiq.org/iqfvp/Pdfs/Vol9%20no%202/RMIQVol9No2_1.pdf

Gibson, I., Rosen, D. W., & Stucker, B. (2010). *Additive manufacturing technologies: Rapid prototyping to direct digital manufacturing*. Springer US. https://doi.org/10.1007/978-1-4419-1120-9

Junk, S., & Kuen, C. (2016). Review of Open Source and Freeware CAD Systems for Use with 3D-Printing. *Procedia CIRP*, *50*, 430–435. https://doi.org/10.1016/j.procir.2016.04.174

Kajtez, J., Buchmann, S., Vasudevan, S., Birtele, M., Rocchetti, S., Pless, C. J., Heiskanen, A., Barker, R. A., Martínez-Serrano, A., Parmar, M., Lind, J. U., & Emnéus, J. (2020). 3D-Printed Soft Lithography for Complex Compartmentalized Microfluidic Neural Devices. *Advanced Science*, *7*(16). https://doi.org/10.1002/advs.202001150

Kaufmann, B. K., Rudolph, M., Pechtl, M., Wildenburg, G., Hayden, O., Clausen-Schaumann, H., & Sudhop, S. (2024). mSLAb – An open-source masked stereolithography (mSLA) bioprinter. *HardwareX*, *19*. https://doi.org/10.1016/j.ohx.2024.e00543

Lapizco-Encinas, B. H. (2008). APLICACIONES DE MICROFLUÍDICA EN BIOSEPARACIONES MICROFLUIDICS APPLICATIONS IN BIOSEPARATIONS. *Revista Mexicana de Ingeniería Química*, *7*(3), 205–214. https://rmiq.org/iqfvp/Pdfs/Vol%207%20no%203/3_RMIQ_Vol7No3_290508.pdf

Leong, K. M., Sun, A. Y., Quach, M. L., Lin, C. H., Craig, C. A., Guo, F., Robinson, T. R., Chang, M. M., & Olanrewaju, A. O. (2024). Democratizing Access to Microfluidics: Rapid Prototyping of Open Microchannels with Low-Cost LCD 3D Printers. *ACS Omega*. https://doi.org/10.1021/acsomega.4c07776

Liu, X., Sun, A., Brodský, J., Gablech, I., Lednický, T., Vopařilová, P., Zítka, O., Zeng, W., & Neužil, P. (2024). Microfluidics chips fabrication techniques comparison. *Scientific Reports*, *14*(1). https://doi.org/10.1038/s41598-024-80332-2

Manapat, J. Z., Chen, Q., Ye, P., & Advincula, R. C. (2017). 3D Printing of Polymer Nanocomposites via Stereolithography. In *Macromolecular Materials and Engineering* (Vol. 302, Issue 9). Wiley-VCH Verlag. https://doi.org/10.1002/mame.201600553

Milovanović, A., Montanari, M., Golubović, Z., Mărghitaş, M. P., Spagnoli, A., Brighenti, R., & Sedmak, A. (2024). Compressive and flexural mechanical responses of components obtained through mSLA vat photopolymerization technology. *Theoretical and Applied Fracture Mechanics*, *131*. https://doi.org/10.1016/j.tafmec.2024.104406

Mishra, P. (2020). Additive Manufacturing (3D Printing): A Review on the Micro fabrication Methods. *International Journal for Research in Applied Science and Engineering Technology*, *8*(4), 956–975. https://doi.org/10.22214/ijraset.2020.4160

Mukherjee, P., Nebuloni, F., Gao, H., Zhou, J., & Papautsky, I. (2019). Rapid prototyping of soft lithography masters for microfluidic devices using dry film photoresist in a non-cleanroom setting. *Micromachines*, *10*(3). https://doi.org/10.3390/mi10030192

Niculescu, A.-G., Chircov, C., Bîrcă, A. C., & Grumezescu, A. M. (2021). Fabrication and Applications of Microfluidic Devices: A Review. *International Journal of Molecular Sciences*, *22*(4), 1–26. https://doi.org/10.3390/ijms22042011

Niedz, R. P., & Evens, T. J. (2016). Design of experiments (DOE)—history, concepts, and relevance to in vitro culture. In *In Vitro Cellular and Developmental Biology - Plant* (Vol. 52, Issue 6, pp. 547–562). Springer New York

LLC. https://doi.org/10.1007/s11627-016-9786-1

Orzeł, B., & Stecuła, K. (2022). Comparison of 3D Printout Quality from FDM and MSLA Technology in Unit Production. *Symmetry*, *14*(5). https://doi.org/10.3390/sym14050910

Razavi Bazaz, S., Rouhi, O., Raoufi, M. A., Ejeian, F., Asadnia, M., Jin, D., & Ebrahimi Warkiani, M. (2020). 3D Printing of Inertial Microfluidic Devices. *Scientific Reports*, *10*(1). https://doi.org/10.1038/s41598-020-62569-9

Ren, K., Zhou, J., & Wu, H. (2013). Materials for microfluidic chip fabrication. *Accounts of Chemical Research*, *46*(11), 2396–2406.

Shahrubudin, N., Lee, T. C., & Ramlan, R. (2019). An overview on 3D printing technology: Technological, materials, and applications. *Procedia Manufacturing*, *35*, 1286–1296. https://doi.org/10.1016/j.promfg.2019.06.089

Sósol-Fernández, R. E., Marín-Lizárraga, V. M., Rosales-Cruzaley, E., & Lapizco-Encinas, B. H. (2012). ANÁLISIS DE CÉLULAS EN DISPOSITIVOS MICROFLUÍDICOS. *Revista Mexicana de Ingeniería Química*. https://rmiq.org/iqfvp/Pdfs/Vol.%2011,%20No.%202/Bio2/Bio2.pdf

Tabeling, P. (2023). *Introduction to Microfluidics*. Oxford University Press.

Talam, S., Avula, K. P., Syed, S., & Battula, S. (2025). Fabrication techniques for microfluidics devices. In *Utilizing Microfluidics in the Food Industry* (pp. 69–96). Elsevier. https://doi.org/10.1016/B978-0-443-13453-1.00004-8

Taylor, A. M., Rhee, S. W., Tu, C. H., Cribbs, D. H., Cotman, C. W., & Jeon, N. L. (2003). Microfluidic multicompartment device for neuroscience research. *Langmuir*, *19*(5), 1551–1556. https://doi.org/10.1021/la026417v

Topcu, O., & Unver, H. O. (2011). *A method for slicing CAD models in binary STL format*. https://www.researchgate.net/publication/259843304

Torres-Alvarez, D., Bosques-Palomo, B., Martínez-Dibildox, A., Marcos-Abdala, A., Jiménez-Nuñéz, R., Morones-Ramírez, J. R., Aeinehvand, M. M., & Aguirre-Soto, A. (2024). Introduction of the lowest printable (channel) characteristic length (LPCL) as a geometrical metric for the SLA 3D printing of embedded negative micro-structures. *Progress in Additive Manufacturing*. https://doi.org/10.1007/s40964-024-00788-6

Tumbleston, J. R., Shirvanyants, D., Ermoshkin, N., Janusziewicz, R., Johnson, A. R., Kelly, D., Chen, K., Pinschmidt, R., Rolland, J. P., & Ermoshkin, A. (2015). Continuous liquid interface production of 3D objects. *Science*, *347*(6228), 1349–1352.

Valizadeh, I., Tayyarian, T., & Weeger, O. (2023). Influence of process parameters on geometric and elasto-visco-plastic material properties in vat photopolymerization. *Additive Manufacturing*, *72*. https://doi.org/10.1016/j.addma.2023.103641

Waldbaur, A., Rapp, H., Länge, K., & Rapp, B. E. (2011). Let there be chip - Towards rapid prototyping of microfluidic devices: One-step manufacturing processes. In *Analytical Methods* (Vol. 3, Issue 12, pp. 2681–2716). https://doi.org/10.1039/c1ay05253e

Wei, C., & Li, L. (2021). Recent progress and scientific challenges in multi-material additive manufacturing via laser-based powder bed fusion. *Virtual and Physical Prototyping*, *16*(3), 347–371.

Whitesides, G. M. (2006). The origins and the future of microfluidics. *Nature*, *442*(7101), 368–373. https://doi.org/10.1038/nature05058

Zhang, J., Hu, Q., Wang, S., Tao, J., & Gou, M. (2020). Digital light processing based three-dimensional printing for medical applications. *International Journal of Bioprinting*, *6*(1), 12–27. https://doi.org/10.18063/ijb.v6i1.242

Zhou, X., Hou, Y., & Lin, J. (2015). A review on the processing accuracy of two-photon polymerization. *AIP Advances*, *5*(3). https://doi.org/10.1063/1.4916886